Aerodynamics of Centrifugal Turbine Cascades

Giacomo Persico
Associate Professor
Laboratorio di Fluidodinamica delle Macchine,
Dipartimento di Energia,
Politecnico di Milano,
via Lambruschini 4,
Milano 20156, Italy
e-mail: giacomo.persico@polimi.it

Matteo Pini
Assistant Professor
Propulsion and Power,
Aerospace Engineering Faculty,
Delft University of Technology,
Delft 2629 HS, The Netherlands
e-mail: M.Pini@tudelft.nl

Vincenzo Dossena
Associate Professor
Laboratorio di Fluidodinamica delle Macchine,
Dipartimento di Energia,
Politecnico di Milano,
via Lambruschini 4,
Milano 20156, Italy
e-mail: vincenzo.dossena@polimi.it

Paolo Gaetani
Associate Professor
Laboratorio di Fluidodinamica delle Macchine,
Dipartimento di Energia,
Politecnico di Milano,
via Lambruschini 4,
Milano 20156, Italy
e-mail: paolo.gaetani@polimi.it

Introduction

Energy conversion systems based on the use of organic fluids, commonly referred to as ORC systems, represent nowadays a mature and cost-effective technology for the efficient exploitation of energy sources characterized by low-to-medium temperature levels [1,2]. As largely documented, see, for instance [3], the performance of ORC systems is mostly dependent on expander efficiency. In order to gain turbine efficiency, the selected machine is usually a turbo-expander for the power range from few kW_{el} up to few MW_{el}, whereas for smaller scale ORC power plants volumetric machines might be more suitable [4].

The specific characteristics of organic fluids generally lead to turbines featuring unusual configurations [3]. Notably, the typical high expansion ratio and low enthalpy drop of ORC fluids imply single- or two-stage turbines, of centripetal [5] or axial-flow [6,7] architecture, often characterized by converging–diverging channels and strong shocks at blade outlet regions. As a result, with respect to present-day steam and gas turbine technology, ORC turbo-expanders are characterized by a relatively low efficiency at nominal point and by a relevant performance penalty at off-design conditions.

The radial outflow, or centrifugal, turbine might help overcoming some of these limitations. The centrifugal architecture, originally conceived by Ljungström [8], can better accomplish the large volumetric flow ratio typical of ORC fluids. Furthermore, many stages can be disposed in a relatively compact machine, thus reducing the stage loading and avoiding supersonic flow conditions. Besides that, the inherent increase of passage area along the flow path limits the flaring angle and then prevents the onset of significant spanwise flow components. These advantages pro-vide a considerable increase of aerodynamic performance at nomi-nal point and greater flexibility at partial loads, as asserted in Refs. [9,10]. Additionally, the low enthalpy drop typical of ORC machines avoids the use of Ljungström counter-rotating solution (originally conceived to provide the high specific work exchange required by the steam technology) and allows classic stator–rotor stage assembly with lesser mechanical complexity. A conceptual prototype of such machine has been recently proposed in Refs. [9,11], and it is receiving scientific as well as industrial recognition.

A research program on novel turbine concepts for ORC applica-tion is presently ongoing at Politecnico di Milano, with the aim of investigating the potential of centrifugal turbine and its range of applicability. Specifically, a design methodology has been con-ceived, first focused on the preliminary design and based on mean-line and throughflow codes [9], and then oriented to the aer-odynamic design of centrifugal turbine blades [12].

However, in the absence of any experimental evidence, a reli-able assessment of the technology can only be based on high-fidelity CFD predictions, which are by now mature to provide accurate estimates of turbine performance, as extensively demon-strated in many research works such as Ref. [13]. Given the nov-elty of the turbine configuration considered here, a detailed study

on three-dimensional aerodynamics of fixed and rotating centrifugal cascades is still not present in the open literature. Radial-outward rows entail many intriguing fluid-dynamic characteristics worthy of research, namely: (i) secondary flows in centrifugal stators may benefit from the absence of the spanwise pressure gradient, which affects axial and mixed-flow machines; (ii) the channel flaring, when positive, may counteract the expansion imparted by the blade deflection if proper 3D blade design is not adopted; (iii) highly nonconventional features characterize the flow in centrifugal rotors, as the specific character of centrifugal cascades couples with the effects of centrifugal and Coriolis forces, with relevant implications on both blade-to-blade flow features and secondary flows. In the present work, all these issues and their impact on losses are investigated in detail, considering the last stage of the transonic centrifugal turbine proposed in Ref. [9].

The paper is laid out as follows. After an overview of the turbine layout, the blade design technique proposed by the authors in Ref. [12] is briefly recalled and applied to the present configuration. The resulting centrifugal turbine stage is then analyzed by applying a high-fidelity Reynolds-averaged Navier–Stokes CFD model, focusing on the three-dimensional flow features and on inertial effects in the rotating blade row.

Layout of a Multistage Centrifugal Turbine

This study has been carried out considering the centrifugal turbine configuration proposed by Ref. [9]. The machine was conceived for application in a (relatively) high-temperature ORC system. Siloxane MDM was selected as working fluid. Operating conditions taken as reference for the design are listed in Table 1.

As one of the key advantages of the centrifugal turbine architecture is the multistage arrangement, a parametric study was initially performed to determine the optimal number of stages. In the framework of the present research program, a preliminary optimization tool was developed by combining an in-house mean-line code, called ZTURBO, with a genetic algorithm [10]. By applying this code several mean-line designs were obtained by optimizing the machine for progressively increasing number of stages. Blade radial chords, discharge flow angles, and stage reaction degrees (assumed identical for all the stages) were used as design variables in the evolutionary optimization process, while the inlet flow angles and the blade span were subsequently computed by the code once the optimal design parameters were found.
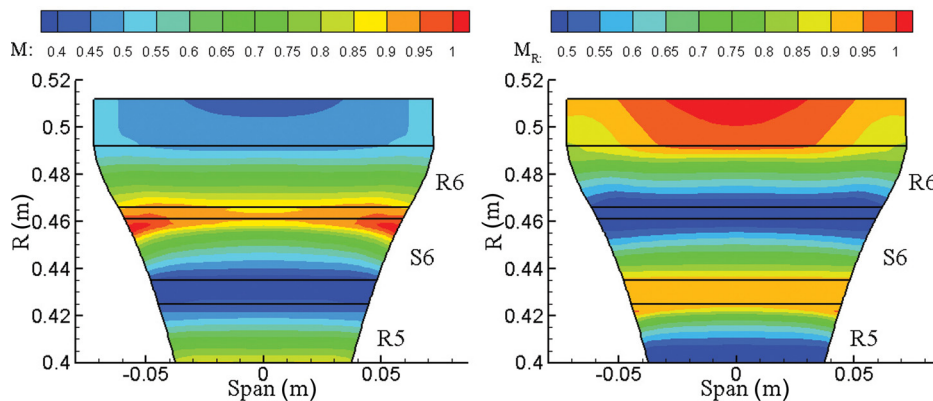
A six-stage machine was eventually identified as the optimal trade off-between compactness and performance, providing an estimated efficiency of 87% with an external diameter of 1 m. The optimal discharge flow angle of all the blade rows is about 67 deg (opposite in sign between stators and rotors), the optimal meridional chord was found to be 26 mm long for each cascade, while the optimal reaction degree resulted of about 0.5. The machines also feature a smooth meridional channel with maximum flaring angle of 30 deg in the last stage. A maximum Mach number equal to 0.99 is reached at the exit section of the last stage rotor, resulting in an unchocked weakly transonic machine.

The optimal machine configuration was subsequently analyzed with the in-house throughflow code TZFLOW [14], which confirmed the expected mean-line features and the overall machine performance [9]. However, relevant spanwise gradients appear in the last stage due to the relatively large flaring. As visible in Fig. 1, which depicts the distributions of absolute and relative Mach number in the last stage on the meridional plane, the flow undergoes excursions in supersonic regime in local regions close to the endwalls of the both the stator and rotor, due to the coupling between streamwise and spanwise pressure gradients.

The resulting highly complex flow configuration is worth detailed aerodynamic investigation with appropriate flow models. Moreover, both the mean-line and throughflow codes make use of correlations (in this case the Craig and Cox model [15]) to account for losses within the blade rows, which need assessment in the present radial-outflow configuration. Eventually preliminary design tools do not provide the detailed shape of the blades, unless standard criteria are available to define the profile shape from the inlet/outlet flow angles (as done, for example, in Ref. [16]); such criteria are of course not available for the present nonconventional machine. The three issues reported above represent the motivation of the present investigation. To properly investigate the cascade aerodynamics and provide reliable estimates of the machine performance high-fidelity CFD is here applied to the sixth stage of the turbine, which is of particular interest, given the fully three-dimensional flow configuration suggested by the throughflow calculations. Prior to the discussion of the computational results, a review of the CFD model applied in this study is first provided in the following Methodology section.

Methodology

The calculations presented in this paper were performed using the ANSYS-CFX code, by applying high-resolution numerical schemes and implicit time integration. Turbulence effects are introduced using the $k - \omega$ SST model, ensuring wall y^+ below unity all along the blade and the endwall, by imposing a proper clustering of the cells in the viscous and buffer sublayers. The thermodynamic behavior of the fluid was modeled with the

Table 1   Turbine design conditions

Fluid	$P_{T,in}$	$T_{T,in}$	P_{out}	Ω	Target power
MDM	10 bar	274 °C	0.17 bar	3000 rpm	1–1.5 MW

Fig. 1   Distribution of absolute and relative Mach number in the last stage of the centrifugal turbine

Span–Wagner Equations of State [17], using a look-up table approach; the tables were constructed by resorting to the external thermodynamic library [18], using pressure and temperature as independent pair, and including tabulated transport properties (molecular viscosity and thermal conductivity). Preliminary trials, performed for transformations occurring in regions where the fluid behaves as an ideal gas, indicated the reliability of the look-up table approach used here.

As usual in subsonic or transonic cascade simulations, total quantities, turbulence quantities, and flow angles are assigned at the inlet, while the static pressure is assigned at the outlet; in centrifugal machines, the annulus region from the blade trailing edge to the outflow boundary acts as a vaneless diffuser, so some iterations were required to identify the proper outflow pressure to achieve the desired expansion ratio on the cascade. Furthermore, since the channel and the boundary conditions are symmetric with respect to the midspan plane (the flaring is equally distributed on the hub and shroud surfaces and no hub or tip clearances are considered), and the blades are untwisted, only half of the span was simulated, assigning a symmetry condition at midspan. Adiabatic no-slip walls are prescribed on the blade and hub surfaces; further simulations with slip conditions assigned on the hub wall were also performed to determine the reference flow for the definition of the secondary field, as discussed later.

Calculations were performed on structured grids composed by hexahedral elements. A grid independent analysis was performed by progressively reducing the grid spacing in the blade-to-blade surface and in spanwise direction, and using the cascade kinetic loss coefficient as convergence monitor (the interested reader is referred to Ref. [12] for a detailed quantitative discussion of the grid independent analysis on the blade-to-blade mesh). An optimal grid configuration was achieved for a grid of about 2.5×10^6 of cells both for the stator and for the rotor cascades, with 50,000 cells in the blade to blade surface and 50 cells in spanwise direction. This relatively high number of elements is motivated by the presence of shocks, and by the significant cell clustering at the profile and end-walls required to guarantee the desired value of y^+. The computational time for each simulation was about 10 hr on 14 (Opteron/AMD) processors at 2.4 GHz and infinite band connection.

The reliability of the numerical model used in this context was previously assessed against experiments performed by the authors themselves on a research turbine stage installed at Politecnico di Milano [13]. The CFD model was shown to accurately predict the fully three-dimensional and unsteady flow physics, and provided estimates of stage efficiency within 1% of the experimental datum, i.e., comparable to the uncertainty of the measurement technique.

Profiles for Centrifugal Turbine Blades

The stator and rotor blade rows studied in this work have been designed by applying the simple but effective technique introduced by the authors in Ref. [12], which is briefly recalled here.

The design of centrifugal turbine profiles is, in fact, a challenging task, since specific design criteria are not available in the open literature for this class of machines. The centrifugal turbine is a novel context in which the available knowledge on centrifugal compressors is almost useless, and the experience gained on axial turbines must be adapted and re-assessed.

Both front- and aft-loaded profiles were considered. These design concepts, developed for axial machines, differ for the distribution of curvature along the blade chord. Typical front-loaded profiles have large curvature in the front part and are almost straight in the rear part; conversely, aft-loaded profiles are curved also in the rear part, leading to a more regular flow acceleration.

Two profiles of these two classes, selected among typical axial turbine blades, were tested and shown to have similar perform-ance in axial turbine configuration; however, when the profiles are tested in the centrifugal configuration, the aft-loaded design outperformed the front-loaded one [12]. The motivation for this different performance lies in the inherent divergent shape of the channel section in centrifugal machine; when straight blades are used, undesired converging–diverging ducts are generated within the cascades, which are a very critical issue in transonic conditions.

As a result, the aft-loaded design concept was adopted in the present study. In order to guarantee a proper control of the profile curvature, the mean-line of the profiles was assigned as an elliptic arc, whose aspect ratio was determined after a parametric optimization. The inlet and outlet geometric angles of the blades were determined from the optimal velocity triangles, with an indication of the flow incidence and deviation angles. In this case, null incidence has been assigned as design rule for the front part of the blade; the deviation was determined using the correlation of Ainley and Mathieson [19], which was shown to provide reliable estimates also for centrifugal cascades [12].

Given the specific character of the radial machine, in which neither radial equilibrium nor variation in peripheral speed affect the flow in spanwise direction, no three-dimensional design concept is used here, and dihedral blades are considered.

Aerodynamics of Centrifugal Turbine Stators

The aerodynamics and performance of a centrifugal turbine stator is discussed in the following, first focusing on the midspan flow and then considering the secondary flows.

To define the blade shape, the thickness distribution was taken from typical slender profiles for low-pressure axial-flow turbines. The blade mean line, instead, was optimized (with a parametric approach) considering the aspect ratio of the elliptic arc as design parameter, leading to an optimal aspect ratio equal to 4.

Blade-to-Blade Flow. Figure 2 shows the midspan flow field of the stator cascade. The analysis of the pressure field, reported on the left frame of the figure, indicates a smooth expansion pro-cess in the blade channel. The gradual curvature of the blade guarantees a regular acceleration of the flow, especially on the blade
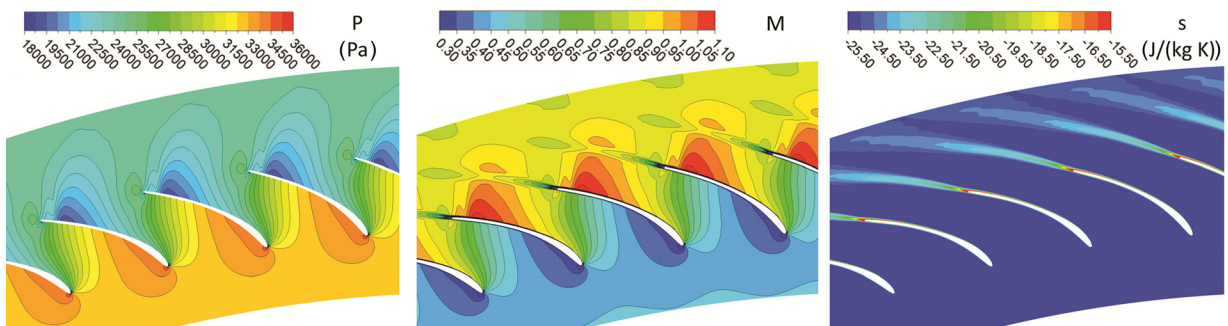

Fig. 2 Blade-to-blade flow in the centrifugal turbine stator

suction side, which allows to avoid choking within the bladed channel. The transonic flow regime and the rear blade curvature lead to the generation of a supersonic zone (maximum Mach number equal to ∼1.1) in the rear blade suction side, as well visible from the Mach number distribution; this eventually brings to the formation of a weak oblique shock just upstream of the trailing edge. The optimization of the blade mean line allows to minimize these supersonic phenomena while guaranteeing the necessary smoothness of the expansion process. As a result, shock entropy production plays a really minor role on the profile losses, which are given just by boundary layer and wake mixing losses as visible in the entropy field reported in the right frame of Fig. 2.

The performance of the blade profile is evaluated by resorting to the kinetic energy loss coefficient at midspan, in a radial position placed 15% of the stator radial chord downstream of the trailing edge (where the leading edge of the downstream rotor is placed). The profile loss coefficient results equal to 2.2%. This value is in line with present-day performance of axial-flow tur-bines and suggests that some relevant aerodynamic concepts developed for axial turbines can be adapted to the radial outflow configuration.

Some interesting features are also found by analyzing the discharge flow angle. By defining the geometric blade angle as the gauging angle $ang_g = \arccos(t/p)$ (where t is the throat and p is the pitch of the cascade), the deviation angle at midspan results of about -1.5 deg; the flow is hence overturned with respect to the geometrical direction. Since the cascade is purely converging, and the flow is not overexpanded downstream of the throat, the overturning is motivated by the blade curvature in the rear part of the profile, which induces a further flow turning with respect to the gauging direction; this effect is explicitly considered by the Ainley and Mathieson correlation [19], which predicts for this case a deviation angle of -1.1 deg, hence in good quantitative agreement with the present result. The flow at the stator exit being highly tangential, an overturning exceeding 1 deg has a significant impact on the velocity component and hence on the work exchange; its estimate is therefore crucial for the design of centrif-ugal turbine stators.

Three-Dimensional Effects and Secondary Flows. The relatively large flaring angle of the present cascade (about 30 deg on both hub and shroud endwalls), the moderate blade aspect ratio and the fairly large endwall boundary layer at the cascade inflow lead to the onset of significant three-dimensional flows. Through-flow simulations, shown in Fig. 1, confirm that in the endwall region the stator flow departs significantly from the two-dimensional midspan distribution.

To better highlight the flow morphology close to the endwalls, and, in particular, to distinguish the inviscid effects of flaring from the viscous ones connected to secondary vortices, two different simulations were performed: (i) a fully three-dimensional calculation (called "fully 3D" in the following), where no-slip conditions are applied on the endwalls and the appropriate endwall boundary layer is assigned at the inflow boundary; (ii) a three-dimensional calculation (called "reference" in the following) where slip conditions are applied on the end-walls and uniform flow is assigned at the inlet, so to inhibit the generation of secondary vortices while retaining the effects of flar-ing and the wake (both the simulations are indeed carried-out with the same turbulence model).

The fully 3D calculation allows to simulate the generation of the secondary flows, which strongly depend on the endwall boundary layer vorticity. The inlet boundary layer was assigned in the form of a spanwise total pressure profile, reported in Fig. 10, which was determined from the entropy field predicted by the throughflow calculation at the sixth stage inlet.

The same computational grid was used for the reference and fully 3D simulations, to ensure the same level of spatial resolution, and very similar convergence trends were found between the two kinds of calculations.

Figure 3 compares the entropy fields at the stator exit for the reference and fully 3D simulations, and also shows in the right frame the spanwise distribution of loss coefficient in the two configurations. As clearly visible from the entropy fields, in the reference flow the only loss mechanism is the wake, which remains uniform all along the span, except for a slight weakening in the wall region below 5% of the blade span. This indicates that the flaring angle, even if relevant, does not trigger significant three-dimensional loss mechanisms and the local acceleration close to the endwall does not lead to the onset of strong shocks in the end-wall region; conversely, the reduction of the wake loss observed in the endwall region is probably connected to a local reduction of blade loading occurring in this region. This feature shows one of the most significant achievements provided by the radial-outflow architecture, which allows to reduce the flaring angle with respect to axial machines and hence to limit three-dimensional losses even in the presence of strong volumetric expansion of the fluid.

A very different picture appears when focusing on the fully 3D calculation, which indicates a wide loss region in the bottom 20% of the blade span; these loss cores are due to the secondary flows generated in the cascade by the deflection applied to the inlet end-wall boundary layer, and eventually lead to a severe increase of loss coefficient in the endwall region.

The character of these three-dimensional effects can be better highlighted by analyzing the secondary velocity vectors and the secondary vorticity fields. To define the secondary flow, the procedure proposed in Ref. [20] was applied. At first, the velocity vector of the fully 3D flow is decomposed according to the
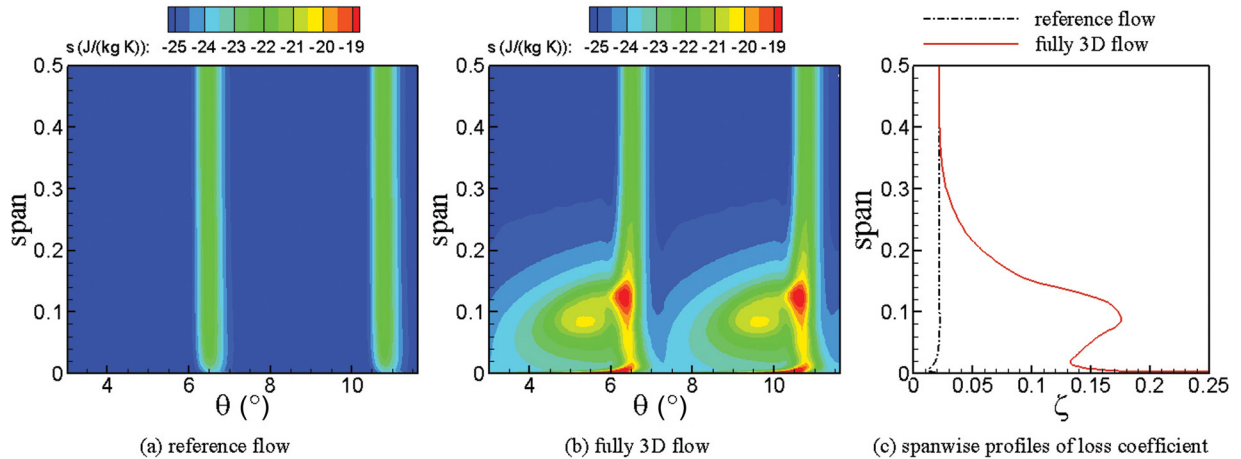

(a) reference flow (b) fully 3D flow (c) spanwise profiles of loss coefficient

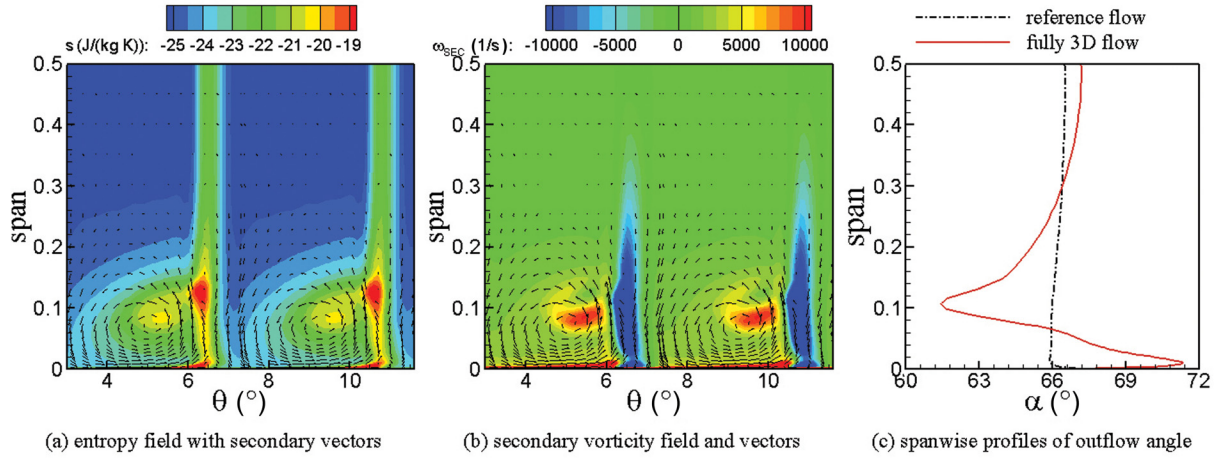**Fig. 3   Entropy field downstream of the stator**

Fig. 4 Secondary vortices and vorticity downstream of the stator

intrinsic coordinate system of the reference flow, which thus is used to identify the streamwise, the normal and binormal directions. The normal and binormal velocity components of the fully 3D calculation constitute the secondary velocity vector, while the secondary vorticity field is determined by projecting the vorticity of the fully 3D calculation along the streamwise direction. Figure 4 provides the secondary velocity vectors superimposed to both the entropy and the secondary vorticity fields, as well as the spanwise distribution of flow angle. The velocity vectors clearly indicate a large-scale counter-clockwise circulation centered at about 10% span, characterized by a positive vorticity and by a wide and diffused loss core. These features are consistent with the stator passage vortex. Close to the passage vortex a narrow region of negative vorticity is observed, corresponding to a local strengthening of the wake and leading to the formation of the strongest loss core. This structure represents the evolution of the vortex sheet generated, downstream of the trailing edge, by the interaction between corotating passage vortices belonging to adjacent passages, often called trailing shed vorticity. The passage vortex dominates the flow angle distribution in the bottom 20% of the span: at the endwall the typical overturning due to the pressure-to-suction crossflow is observed, followed by a large underturning region above 10% of the span. It is interesting to note how a residual effect of the endwall flows is also found at midspan, where the flow angle is slightly higher (about 0.5 deg) than that observed for the reference flow. However the relevant underturning affecting a considerable portion of the span eventually leads to a reduction of mean overall flow angle, which goes from 66.3 deg for the reference flow to 66.0 deg for the fully 3D configuration.

As a consequence of the secondary effects, the overall loss coefficient grows significantly with respect to the reference value. Considering the mixed-out values, the loss coefficients results 3.2% for the reference flow, and it raises to 4.8% in the fully 3D configuration. For comparison, the Craig and Cox loss correlation [15], developed for axial turbines and also used for the preliminary design of the present turbine, predicts a cascade loss coefficient of about 7.3%. This finding is a promising outcome of the high-fidelity calculation and confirms the potential of centrifugal turbines for this application.

Aerodynamics of Centrifugal Turbine Rotors

The specific features that characterize the stator of a centrifugal turbine are expected to be even more significant for the rotor, since in radial machines the effect of inertial forces (also referred to as rotation effect) plays a more relevant role than in axial machines. As a matter of fact, in radial machines both the centrifugal and Coriolis forces act on the blade-to-blade plane, with relevant implications on the work exchange process and on the aerodynamics of the blade row. Moreover, as shown in the following, the rotation also influences the secondary flows generated in the cascade.

To highlight the rotation effect, rotating-frame CFD simulations on the rotor are compared to several calculations performed in a fixed-reference frame (providing consistent boundary conditions). Fully 3D simulations and reference flow simulations were performed, as done for the stator, to rigorously determine the secondary flow. Considering all the tested configurations, a set of seven different calculations was performed, briefly recalled in Table 2. To support the reader's comprehension, the flow model as well as the synthetic motivation for each calculation is also reported.

The rotor blade geometry was optimized by applying the same procedure described for the stator: the thickness distribution used for the stator was retained, while for the elliptic-arc meanline an optimal aspect ratio equal to 2 was identified after a dedicated parametric optimization. It should be noted that the rotor design was carried-out using a fixed reference frame setup, in order to better highlight the impact of the inertial forces on the rotor blade aerodynamics. No three-dimensional design concepts

Table 2 Summary of the simulated rotor configurations

Case name	Rotation	3D model	Inflow condition	Motivation
ROT	Yes	Fully 3D	Absolute flow at stator-exit	Rotor aerodynamics
ROT-REF	Yes	Reference	Absolute flow at stator-exit (uniform)	Reference in rotation
FIX-LE	No	Fully 3D	Relative flow at rotor inlet	Removal of rotation effect
FIX-LE-SV	No	Fully 3D	Relative flow with stator-like endwall vorticity	Impact of endwall vorticity
FIX-LE-REF	No	Reference	Relative flow at rotor inlet (uniform)	Reference for fixed cascade
FIX-TE	No	Fully 3D	Relative flow with peripheral speed at rotor TE	Impact of centrifugal force
FIX-TE-REF	No	Reference	Relative flow with peripheral speed at rotor TE (uniform)	Reference for fixed cascade
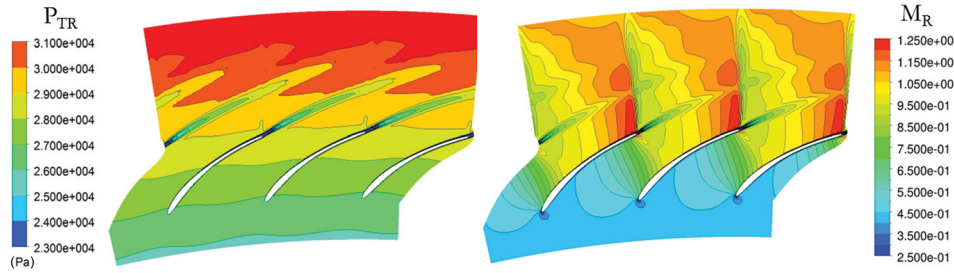
Fig. 5 Relative total pressure and Mach number distributions on the rotor blade row at midspan—ROT CASE

were applied for the spanwise design, the airfoil resulting in a dihedral blade with constant profile along the span.

In the following the midspan flow is first analyzed, and then the secondary field is discussed.

Rotation Effect on the Blade-to-Blade Flow at Midspan.
Figure 5 depicts the distribution of relative total pressure and relative Mach number at midspan for the rotating-frame calculation. Relative Mach number exceeding 1.2 is predicted on the rear suction side of the blade, resulting in a relatively strong shock on the trailing edge of the blade. Relevant differences arise with respect to the stator cascade (see Fig. 2), in terms of shock strength and position, even though the expansion ratio and the shape of the two blades are very similar. The motivation of these differences can be found by observing the distribution of relative total pressure field on the blade-to-blade plane, also reported in Fig. 5, which shows a progressively increasing relative total pressure moving from inlet to outlet of the cascade. This is due to the centrifugal force, which tends to increase the relative mechanical energy of the fluid in the radial outward direction simply because of the increase of peripheral speed in the meridional direction. With respect to axial machines, in the present configuration the variation of centrifugal force affects the profile aerodynamics and not the spanwise evolution of the flow; as a result, while approaching the trailing edge of the blade, the overspeed on the suction side exceeds the one that would occur in a fixed cascade or in an axial turbine rotor, resulting in a significant change of the pressure distribution on the blade and eventually on the shock strength.

In order to quantify the effect of the centrifugal force, two simulations in the fixed reference frame were performed. These calculations require the relative total pressure and the relative total temperature as inflow boundary conditions taken from the rotating frame simulation. The first calculation was then carried out by assigning the relative total quantities evaluated on the blade leading edge, whereas the second one by assigning total quantities evaluated on the trailing edge. The relative inlet flow angle was assigned in both the calculations aligned with the rotor-inlet

metallic angle, as occurs in the rotating-frame calculation. Finally, the static pressure at the outflow boundary was assigned matching the design discharge conditions of the turbine.

Figure 6 shows the Mach number distribution predicted by the two fixed simulations; a comparison with the field reported in Fig. 5 clearly shows that both the fixed calculations fail in representing the actual flow configuration. The calculation performed for leading edge total quantities is characterized by a smaller supersonic bubble and by a very weak shock upstream of the trailing edge, similarly to what observed for the stator (see Fig. 2). The calculation performed using the trailing edge total quantities is qualitatively similar to the previous one apart from a maximum Mach number and a shock strength similar to that of the rotating simulation. However, the shape and the extension of the supersonic region are not properly captured, and the position of the shock at the trailing edge is not correctly represented.

Figure 7 shows the isentropic Mach number distribution for the three rotor calculations at midspan. The differences observed in the flow field mostly affect the pressure distribution on the rear suction side, where the overspeed for the rotating calculation is not captured both in terms of magnitude and position. This is particularly visible when using leading edge relative total quantities as inflow condition. The calculation with trailing edge total quantities provides a better estimate of the maximum overspeed, but still in an upstream position with respect to that found for the rotating-frame calculation. As a matter of fact, in this latter configuration, the overspeed occurs just at the trailing edge, because the relative total pressure raises continuously along the blade due the centrifugal force; as a result, the isentropic Mach number at the exit is higher than that found for both the fixed calculations, regardless the values of total quantities assigned at the inlet.

Beside the dominant role of the centrifugal force on centrifugal rotors, also the Coriolis force has an impact on the rotor aerodynamics. As is well known, in centrifugal compressors the Coriolis force generates a relative-frame vortex acting on the blade-to-blade plane, which turns the discharge flow angle in opposite direction with respect to the peripheral speed; this leads to a reduction of work exchange, usually measured through the
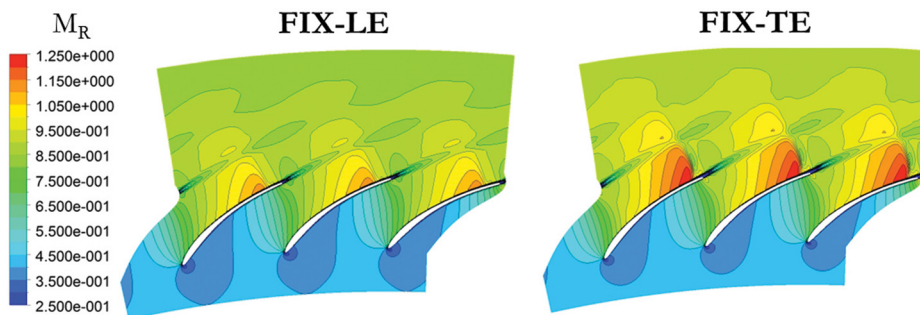
Fig. 6 Relative Mach number distributions on the rotor blade row removing inertial effects. Left frame: FIX-LE case; right frame: FIX-TE case.
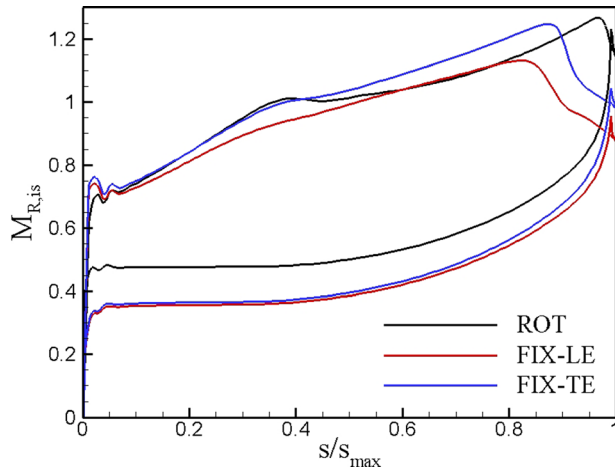
Fig. 7 Isentropic relative Mach number distributions for the inertial and noninertial models

Table 3 Midspan flow properties at the rotor exit

Configuration	β (deg)	α (deg)	ζ_{mix} (%)
Fixed-LE	−67.2	45.7	2.82
Fixed-TE	−66.7	32.5	3.30
Rotating	−67.8	37.7	4.90

so-called "slip factor" (see Ref. [21] for a review on the slip factor correlations presently available). In centrifugal turbines, the same physical mechanism observed in compressors is expected to occur, but with opposite implications. An analysis of the relative velocity vector and of the angular speed indicates that the Coriolis force acts so as to further deflect the flow in the tangential direction, thus providing a negative contribution to the rotor blade deviation and eventually leading to an increase of work exchange.

Table 3 reports about the relative and the absolute flow angles evaluated at midspan 15% of the radial chord downstream of the rotor trailing edge, in the near-wake zone. The mixed-out loss coefficient at midspan is also reported to quantify the impact of the rotating effect on the cascade performance.

The overall results indicate that the rotating calculation actually predicts a more tangential flow discharged by the rotor, and confirm that the Coriolis force is driving the flow in the opposite direction with respect to the rotor velocity. Considering the fixed calculation with trailing edge inflow conditions, which provides the most accurate pressure distribution on the profile out of the two fixed calculations, the quantitative impact of the rotation effect exceeds 1 deg. This value of overturning, apparently small with respect to the typical slip values observed in radial compressors, leads to a significant change of relative velocity magnitude as it is added to a highly tangential flow. The corresponding absolute flow angle changes indeed by 5 deg from fixed to rotating simulations, with a significant impact on the work exchange.

The loss coefficients also indicate that the rotation has a relevant impact on the cascade performance; this is essentially due to the centrifugal force, most of the difference in losses being due to the weaker shock predicted in both the fixed calculations.

These results suggest that reliable predictions of the rotation effects can be only achieved by means of rotating frame simulations. As a consequence, an appropriate blade design of centrifugal turbine rotors should consider inertial phenomena in order to match the target velocity triangles with the proposed blade shape.

Rotation Effect on the Secondary Flows. As discussed previously, wide secondary flows are generated in the last stage stator,

as a result of the endwall boundary layer thickening along the turbine meridional channel. In the last stage rotor, the rotation effect could also influence the morphology of the secondary field; to this end, calculations performed in both fixed and rotating reference frames were carried out.

The rotating-frame calculation was performed by assigning at the inflow boundary the spanwise profiles of absolute flow angle and absolute total pressure computed downstream of the stator by the fully 3D simulation, corresponding to the pitchwise averaged profiles shown in Figs. 3 and 4, respectively. As the code solves for the equations expressed in terms of relative velocity, the span-wise profiles of relative flow quantities are automatically deter-mined by code from the assigned absolute ones.

Relative flow profiles are instead required for fixed reference frame simulations. To guarantee full coherence between the fixed and rotating simulations, the inlet relative flow computed by the rotating simulation was assigned at the inlet of the fixed one. For each tested configuration, both reference and fully 3D calculations were carried out in order to properly define the secondary field in all the cases.

The results of the rotating calculation are first discussed. Figure 8 depicts the distribution of the entropy field for the refer-ence and the fully 3D flows on a section placed 15% of the radial chord downstream of the rotor trailing edge, alongside the span-wise distribution of mass-averaged loss coefficient at the same position. The traces of the wake and of the shock can be clearly identified in the two entropy field in the midspan region. The ref-erence flow field indicates a progressive weakening of the wake and shock losses toward the endwall, suggesting a reduction of blade loading in the flaring region of the channel. The fully 3D simulation shows, instead, a significant entropy rise at the end-wall, especially in the wake where the trailing shed vorticity leads to a significant strengthening of the wake loss with respect to the midspan value. No local loss cores are observed outside the wake, differently from what found downstream of the stator (see Fig. 3).

Figure 9 reports the secondary velocity vector, the secondary vorticity and the spanwise distributions of relative flow angles downstream of the rotor. These distributions indicate the presence of a strong positive vorticity in the endwall part of the wake, cor-responding to a narrow counterclockwise vortex, which can be identified as the trailing shed vorticity. In the freestream above, the endwall the secondary velocity vectors also indicate a very weak clockwise circulation, consistent with that of a very weak rotor passage vortex. Close to the wall the velocity vectors indi-cate the typical crossflow from pressure to suction side, but this does not lead to the generation of a well defined vortex core on the suction side of the wake (as instead observed for the stator). The resulting flow angle distribution reveals the overturning at the wall but not the underturning at higher spans (it should be noted that the over- and underturning is here meant with respect to the reference flow).

These results suggest that significant differences do exist between the stator and the rotor secondary fields. Considering that the level of loading of the two cascades is similar, the explanation of these differences has to be found in the rotation effect or in the inflow boundary layer profile. A detailed analysis of the endwall flow reveals that the relative flow entering the rotor is indeed very different from the absolute one entering the stator. Due to vecto-rial composition with the high peripheral speed of the last rotor, the relative velocity in the endwall boundary layer is enhanced. This induces a significant reduction of relative total pressure gra-dient at the rotor inlet and ultimately weakens the relative vortic-ity in the endwall boundary layer.

Figure 10 compares the inlet boundary conditions assigned to the stator and the rotor calculations in terms of total pressure coef-ficient C_{PT}, evaluated by using the absolute total pressure for the stator and the relative total pressure for the rotor. To aid the reader in the quantitative comparison, the profiles are made nondimen-sional by using the same reference, namely, the midspan dynamic pressure at the stator inlet. The trends shown in Fig. 10 confirm
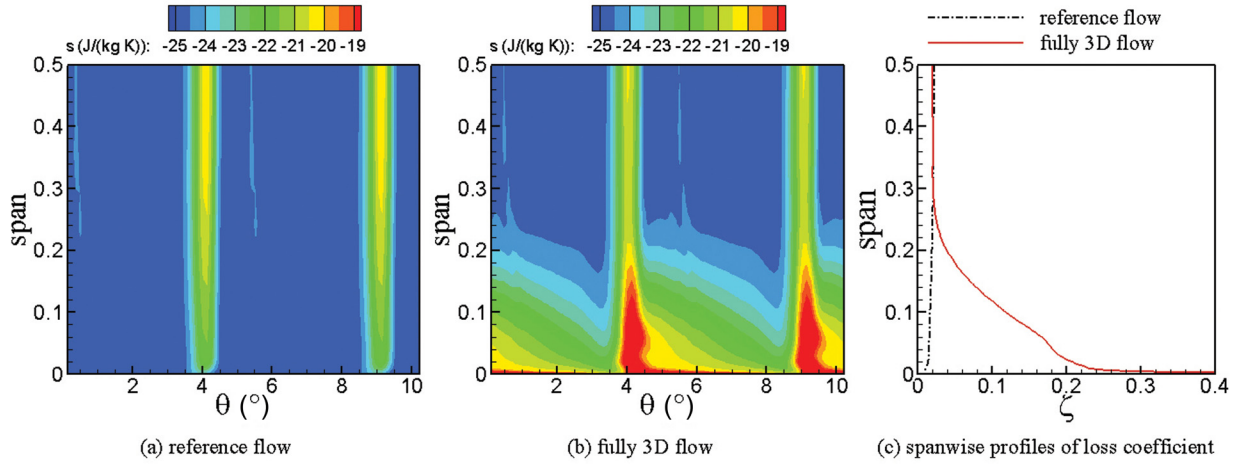
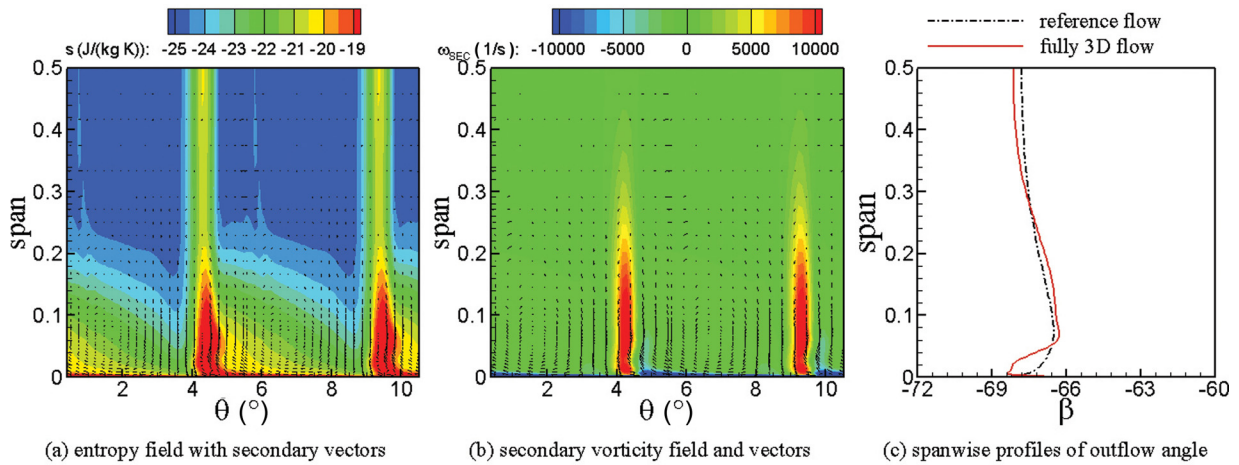**Fig. 8 Entropy field downstream of the rotor with rotation effects**

(a) reference flow
(b) fully 3D flow
(c) spanwise profiles of loss coefficient

Fig. 9 Secondary vortices and vorticity downstream of the rotor with rotation effects

(a) entropy field with secondary vectors
(b) secondary vorticity field and vectors
(c) spanwise profiles of outflow angle

the significant reduction of inlet vorticity when switching from the stator to the rotor configurations, thus justifying the much weaker secondary flows generated in the rotor with respect to those in the stator. As a further proof, the secondary flow
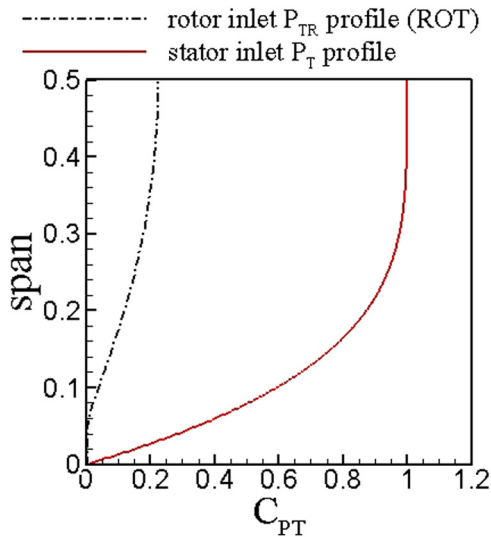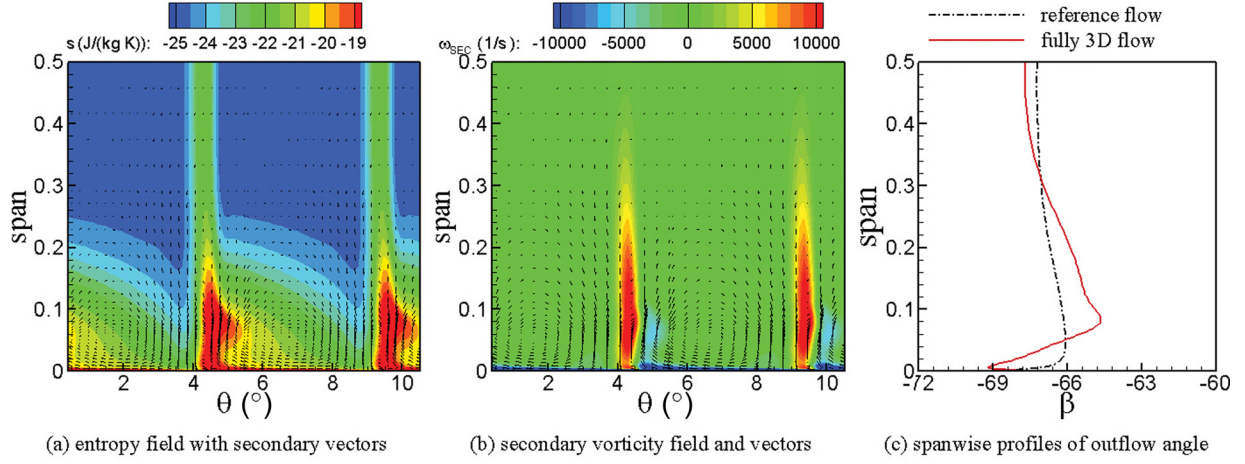

Fig. 10 Spanwise profiles of inlet total pressure at the stator (absolute) and rotor (relative) calculations

predicted by the fixed-reference frame calculation and shown in Fig. 11 is very similar to the one computed for the rotating model.
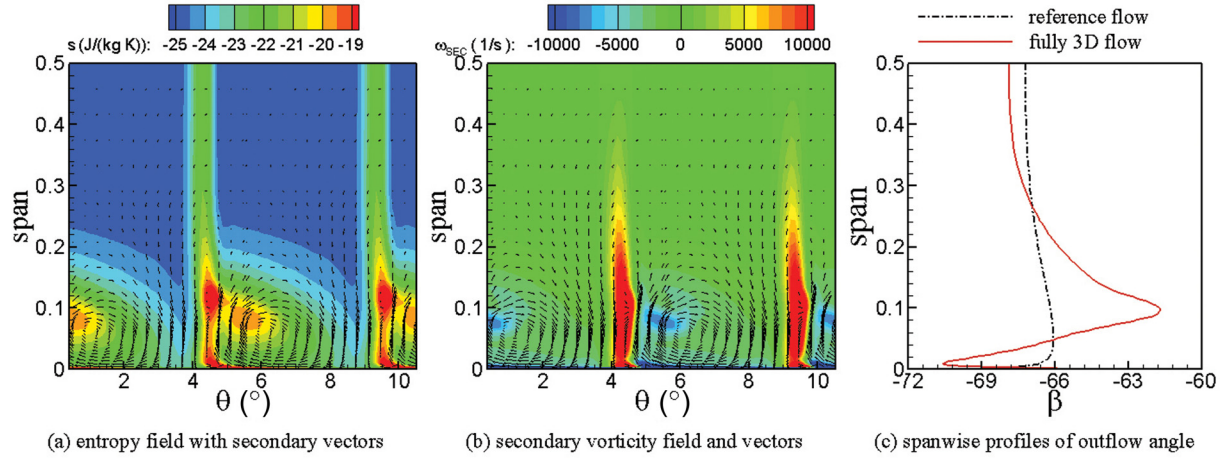
To address the quantitative relevance of the inlet vorticity, a further fixed-reference frame calculation was performed by assigning at the inlet uniform relative total temperature and uniform relative flow angle (corresponding to null incidence on the rotor blade), thus converting the whole inlet entropy gradient into relative total pressure gradient. In this way, the magnitude of the inlet endwall vorticity is much higher than that assigned to the rotating simulation and is very similar to that assigned to the stator. The results, provided in Fig. 12, show a secondary field similar to that found at the stator exit, characterized by well defined loss and vorticity cores and by a large underturning. The comparison between the flow fields in Figs. 11 and 12 clearly indicates that, when modeling the aerodynamics of centrifugal rotors, atten-tion should be paid on the accurate estimate of the rotor inlet boundary layer vorticity.

A further analysis reveals that some differences exists between the secondary fields predicted by the fixed and rotating simulations, even if the same inlet vorticity profiles are assigned. This suggests that the rotation effect has a direct influence also the secondary flows. The way in which the rotation can affect the secondary flow can be theoretically shown by resorting to the equations for the vorticity generation in intrinsic coordinates [22]. Intrinsic coordinates can be defined as the streamwise direction **s**, aligned with the relative velocity, the binormal direction **b**, aligned with the axis of rotation for radial machines, and the normal direction **n**, orthogonal to the other ones. Using this nomenclature, the inlet

(a) entropy field with secondary vectors (b) secondary vorticity field and vectors (c) spanwise profiles of outflow angle

Fig. 11 Secondary vortices and vorticity downstream of the rotor computed in fixed reference frame—real inlet endwall vorticity

(a) entropy field with secondary vectors (b) secondary vorticity field and vectors (c) spanwise profiles of outflow angle

Fig. 12 Secondary vortices and vorticity downstream of the rotor computed in fixed reference frame—high inlet endwall vorticity

endwall vorticity is aligned with the normal direction ($\boldsymbol{\omega} \cdot \mathbf{n} = \omega_n$), while the relative vorticity connected to the angular speed (which causes the slip effect through the Coriolis force) is aligned with the binormal direction ($\boldsymbol{\Omega} = \Omega \mathbf{b}$). In general, in turbomachinery, the secondary vorticity ω_{SEC} can be very well approximated by the streamwise vorticity ω_s, whose generation process can hence be studied to investigate the generation of secondary flows. By assuming steady, inviscid and incompressible flow, and considering a purely radial machine, the equation for the streamwise vorticity generation can be written as

$$\frac{\partial}{\partial s}\left(\frac{\omega_s}{\rho W}\right) = \frac{2\omega_n}{\rho W r} - 2\frac{\boldsymbol{\Omega} \times \boldsymbol{\omega} \cdot \mathbf{s}}{\rho W^2} = \frac{2}{\rho W r}\frac{\partial W}{\partial b} - \frac{2\Omega}{\rho W^2}\frac{\partial W}{\partial b} \quad (1)$$

Equation (1), even though derived under some simplifying hypotheses, suggests two main mechanisms for the generation of streamwise vorticity in rotating cascades: (i) the deflection of endwall boundary layer ω_n (first term of the right hand side expression); (ii) the Coriolis force applied to the normal incoming vorticity in the boundary layer (second term of the right hand side expression). While the first term represents the typical secondary flow generation mechanism, also valid for stationary cascades, the second one provides the basic mechanism of the rotation effect on secondary flows. It is to be noted that such a term is negligible in axial-flow turbines, for that $\boldsymbol{\Omega}$ is almost normal to $\mathbf{b}$; the rotation

effect on the secondary flow is therefore a specific feature of centrifugal turbines.

The present calculations confirm that the rotation influence the rotor secondary flows with respect to the rotating case, the fixed-reference frame calculation shows a stronger passage vortex, with more distinct loss and (negative) vorticity cores on the suction side of the wake, combined to a now visible underturning in the relative flow angle. Conversely the overturning at the endwall is similar for the fixed and rotating simulations. The different features of the secondary flows are consistent with the analysis of the vorticity equation, and can be physically interpreted by considering the different action of the Coriolis force inside and outside the endwall boundary layer: in the boundary layer the Coriolis force (which depends on the magnitude of the relative velocity) is smaller than in the freestream, and has a minor impact on the crossflow; outside the boundary layer the Coriolis force turns the relative flow in tangential direction, acting against the underturning of the secondary flows. As a consequence, the rotation effect weakens, or even prevents, the formation of the passage vortex and almost nullifies the secondary deviation, making the fully 3D flow angle distribution very similar to that of the reference flow (except for the cross flow in 5% of the span closer to the wall).

The secondary losses, computed as entropy production from inlet to outlet of the rotor to eliminate the contribution of the inlet endwall boundary layer, amount to half a point for the fixed

reference frame simulation, and are further reduced by the rotation effect. As a result, secondary losses are one order of magnitude lower than the profile losses in the rotor assembly. Classic correlations developed for axial turbines would instead predict profile and secondary losses of the same order of magnitude for the present cascade, leading to the underestimation of the rotor performance.

Considering that both the stator and rotor cascades were found to be more efficient with respect to the prediction of the correlations, an increase in the full stage performance is expected. In particular, the evaluation of the stage performance based on the present CFD results indicates a total–total isentropic efficiency of the sixth stage of about 93.7%, two points higher than the value of 91.7% estimated by the ZTURBO and TZFLOW codes by using the Craig and Cox correlation. Considering the intrinsic higher fidelity of the CFD model, especially in case of such nonconventional configuration, this outcome suggests that the potential of centrifugal turbines could be even higher than that predicted in earlier studies.

Conclusions

In this paper the aerodynamics of a centrifugal turbine stage have been discussed in detail, considering the effects of the radial-outflow configuration and of the inertial forces in the rotor.

After a brief review of the turbine layout under consideration, a blade design technique specifically developed for centrifugal turbine blades has been discussed and applied to the present configuration. The resulting stage has been analyzed by focusing first on the blade-to-blade aerodynamics and then on the morphology of secondary flows. The flowfield evolving in the centrifugal arrangement is found to be characterized by uncommon features that never occur in conventional axial or centripetal turbines. This particular flow behavior notably impacts on the performance of the machine.

The diverging shape of the bladed channel and the centrifugal force are observed to alter significantly the pressure distribution on the profile. This suggests that specific design criteria are required for the shape optimization of centrifugal turbine blades. The Coriolis force acts to induce a slip effect, similar to that observed in centrifugal compressors, which should be properly modeled to provide reliable estimates of the rotor-exit flow angle. The centrifugal architecture is also found to affect the secondary flows. Thanks to the limited flaring and the almost uniform spanwise pressure distribution provided by the centrifugal configuration, very weak spanwise variations of blade loading are achieved, with beneficial effects on the three-dimensional performance of the cascades. In the rotor the low inlet endwall vorticity and the Coriolis force further weaken the secondary flows, resulting in comparatively low secondary losses with respect to that predicted by loss models developed for axial turbines.

Finally the CFD model predicts a stage efficiency two points higher than that estimated by applying preliminary design tools. This provides a more reliable assessment of the potential of centrifugal turbines for ORC applications. However further numerical and experimental studies are required to establish predictive models for loss and deviation, especially including the initial stages of the machine in which the effects of the radial outward configuration should be further amplified. From this perspective the relevance of the rotation effect demonstrated by the results of this study clearly indicates that simulations and experiments in rotating cascades are crucial to achieve a proper representation of the flow in centrifugal turbines.

Nomenclature

b, pi, o = blade chord, cascade pitch, cascade throat

$C_{\mathrm{PT}} = \dfrac{P_{\mathrm{T}} - P_{\mathrm{T,w}}}{P_{\mathrm{T,FS}} - P_{\mathrm{T,w}}}$ = total pressure coefficient (for stators)

$C_{\mathrm{PT}} = \dfrac{P_{\mathrm{TR}} - P_{\mathrm{TR,w}}}{P_{\mathrm{T,FS}} - P_{\mathrm{T,w}}}$ = total pressure coefficient (for rotors)

$\mathrm{gau} = \arccos \dfrac{o}{pi}$ = gauging angle (here used as geometric angle)

h, s = entropy, enthalpy

M, M_{R} = absolute and relative Mach number

P, T, ρ = pressure, temperature, density

$\mathbf{s}, \mathbf{n}, \mathbf{b}$ = streamwise, normal, and binormal unit vectors

V, W = absolute and relative velocity magnitude

α, β = absolute and relative blade-to-blade flow angle

$\zeta = 2\dfrac{h - h_{\mathrm{is}}}{V_{\mathrm{out}}^2}$ = kinetic energy loss coefficient (for stators)

$\zeta = 2\dfrac{h - h_{\mathrm{is}}}{W_{\mathrm{out}}^2}$ = kinetic energy loss coefficient (for rotors)

$\zeta_{\mathrm{mix}} = 2\dfrac{h_{\mathrm{mix}} - h_{\mathrm{is_{mix}}}}{V_{\mathrm{out_{mix}}}^2}$ = kinetic mixed-out energy loss coefficient (for stators)

$\zeta_{\mathrm{mix}} = 2\dfrac{h_{\mathrm{mix}} - h_{\mathrm{is_{mix}}}}{W_{\mathrm{out_{mix}}}^2}$ = mixed-out kinetic energy loss coefficient (for rotors)

$\boldsymbol{\omega}$ = vorticity vector (absolute in stators, relative in rotors)

$\boldsymbol{\Omega}$ = angular speed

Subscripts

FS = freestream at midspan value

in, out = inlet, outlet conditions

is = isentropic conditions

mix = mixed-out conditions

s, n, b = streamwise, normal, and binormal components

SEC = secondary component

T = total conditions

w = endwall value

References

[1] Angelino, G., Gaia, M., and Macchi, E., 1984, "A Review of Italian Activity in the Field of Organic Rankine Cycles," International VDI Seminar on ORC-HP-Technology, Working Fluid Problems, Zurich, Sept. 10–12, pp. 465–482.

[2] Gaia, M., 2011, "30 Years of Organic Rankine Cycle Development," First International Seminar on ORC Power Systems, Delft, The Netherlands, Sept. 11–23, Keynote Lecture, http://www.orc2011.nl/content/keynote

[3] Macchi, E., 2013, "The Choice of Working Fluid: The Most Important Step for a Successful Organic Rankine Cycle (and an Efficient Turbine)," Second International Seminar on ORC Power Systems, Rotterdam, Oct. 7–8, Keynote Lecture, http://www.asme-orc2013.nl/content/keynote

[4] Oudkerk, J., Quoilin, S., Declaye, S., Guillaume, L., Winandy, E., and Lemort, V., 2013, "Evaluation of the Energy Performance of an Organic Rankine Cycle-Based Micro Combined Heat and Power System Involving a Hermetic Scroll Expander," ASME J. Eng. Gas Turbines Power, **135**(4), p. 042306.

[5] Hoffren, J., Talonpoika, T., Larjola, J., and Siikonen, T., 2002, "Numerical Simulation of Real-Gas Flow in a Supersonic Turbine Nozzle Ring," ASME J. Eng. Gas Turbines Power, **124**(2), pp. 395–403.

[6] Verneau, A., 1987, "Small High Pressure Ratio Turbines," *Supersonic Turbines for Organic Rankine Cycles From 3 to 1300 kW* (Lecture Series No. 1987-07), von Karman Institute for Fluid Dynamics, Sint-Genesius-Rode, Belgium.

[7] Colonna, P., Harinck, J., Rebay, S., and Guardone, A., 2008, "Real-Gas Effects in Organic Rankine Cycle Turbine Nozzles," J. Propul. Power, **24**(2), pp. 282–294.

[8] Ljungstrom, F., 1949, "The Development of the Ljungström Steam Turbine and Air Preheater," Proc. Inst. Mech. Eng., **160**(1), pp. 211–223.

[9] Pini, M., Persico, G., Casati, E., and Dossena, V., 2013, "Preliminary Design of a Centrifugal Turbine for ORC Applications," ASME J. Eng. Gas Turbines Power, **135**(4), p. 042312.

[10] Casati, E., Vitale, S., Pini, M., Persico, G., and Colonna, P., 2014, "Centrifugal Turbines for Mini-Organic Rankine Cycle Power Systems," ASME J. Eng. Gas Turbines Power, **136**(12), p. 122607.

[11] Spadacini, C., Centemeri, L., Xodo, L., Astolfi, M., Romano, M., and Macchi, E., 2011, "A New Configuration for Organic Rankine Cycles Power Systems," First International Seminar on ORC Power Systems, Delft, The Netherlands, Sept. 11–23.

[12] Persico, G., Pini, M., Dossena, V., and Gaetani, P., 2013, "Aerodynamic Design and Analysis of Centrifugal Turbine Cascades," ASME Paper No. GT2013-95770.

[13] Persico, G., Mora, A., Gaetani, P., and Savini, M., 2012, "Unsteady Aerodynamics of a Low Aspect Ratio Turbine Stage: Modeling Issues and Flow Physics," ASME J. Turbomach., **134**(6), p. 061030.

[14] Persico, G., and Rebay, S., 2012, "A Penalty Formulation for the Throughflow Modeling of Turbomachinery," Comput. Fluids, **60**, pp. 86–98.

[15] Craig, H. R. M., and Cox, H. J. A., 1971, "Performance Estimation of Axial Flow Turbines," Proc. Inst. Mech. Eng., **185**(1), pp. 407–424.

[16] Pasquale, D., Persico, G., and Rebay, S., 2014, "Optimization of Turbomachinery Flow Surfaces Applying a CFD-Based Throughflow Method," ASME J. Turbomach., **136**(3), p. 031013.

[17] Colonna, P., Nannan, N., and Guardone, A., 2008, "Multiparameter Equations of State for Siloxanes: $[(CH_3)_3–Si–O_{1/2}]_2–[O–Si–(CH_3)_2]_{i=1,3}$, and $[O–Si–(CH_3)_2]_6$," Fluid Phase Equilib., **263**(2), pp. 115–130.

[18] Colonna, P., and van der Stelt, T. P., 2004, "FluidProp: A Program for the Estima-tion of Thermo Physical Properties of Fluids," Asimptote, Delft, The Netherlands.

[19] Ainley, D. G., and Mathieson, G. C. R., 1952, "A Method of Performance Estimation for Axial-Flow Turbines," Aeronautics Research Council (ARC), London, Technical Report No. 2974.

[20] Persico, G., Gaetani, P., Dossena, V., D'Ippolito, G., and Osnaghi, C., 2009, "On the Definition of Secondary Flows in Three-Dimensional Cascades," Proc. Inst. Mech. Eng., Part A, **223**(6), pp. 667–676.

[21] von Backstrom, T. W., 2006, "A Unified Correlation for Slip Factor in Centrifugal Impellers," ASME J. Turbomach., **128**(1), pp. 1–10.

[22] Horlock, J., and Lakshminarayana, B., 1973, "Generalized Expression for Secondary Vorticity Using Intrinsic Coordinates," J. Fluid Mech., **59**(1), pp. 97–115.